An Impedance-Based Internal Force Coordination Control Method for Dual-Shaking Table Arrays

Wei Guo , Xin Li , Ce Shi , Jinhong Li , Zemin Sun , Yongjia Xu *

Posted Date: 15 April 2026

doi: 10.20944/preprints202604.1109.v1

Keywords: dual-shaking table array; rigid connection; system synchronization; force-based impedance control; internal force coordination

 doi:10.20944/preprints202604.1109.v1

Article

An Impedance-Based Internal Force Coordination Control Method for Dual-Shaking Table Arrays

Wei Guo [1,2,3], Xin Li [1,3], Ce Shi [3], Jinhong Li [1,3], Zemin Sun [1,3] and Yongjia Xu [1,2,3,*]

[1] National Engineering Research Center of High-speed Railway Construction Technology, Changsha 410075, China

[2] China Railway Group Limited, Beijing 100039, China

[3] School of Civil Engineering, Central South University, Changsha 410075, China

* Correspondence: xuyongjia0904@163.com

Abstract

Shaking tables are critical facilities for simulating seismic effects via ground motion reproduction. However, single-table tests are often constrained by limited platform dimensions and load capacity. While multi-table synchronization overcomes these bottlenecks, traditional array control methods under rigid connections face challenges, including degraded precision from desynchronization and experimental interruptions due to output forces exceeding safety limits. To address high-precision synchronization requirements for rigid-connected dual-table arrays, this study proposes an impedance-based internal force coordination control strategy. This approach enhances synchronization accuracy and prevents failures from excessive coupling forces. Specifically, a global simulation model and a mechanical model of the dual-shaking table array under rigid connection were established. Through simulation and experimental validation, the impact of synchronization errors was evaluated and the strategy's efficacy verified. Results show the strategy significantly reduces force discrepancy between platforms. In simulation and experiments, average force discrepancy reductions reached 95.4% and 76.1%, respectively. Both displacement reproduction accuracy and synchronization precision improved. The method effectively circumvents experimental bottlenecks, such as output force saturation, inherently associated with rigid connections.

Keywords: dual-shaking table array; rigid connection; system synchronization; force-based impedance control; internal force coordination

1. Introduction

Shaking tables are specialized facilities designed to simulate seismic actions by reproducing ground motion during earthquakes. These systems are widely utilized in seismic loading tests for various engineering structures[1–3]. Conventional shaking table tests typically employ a single platform; however, constraints such as platform dimensions and load-bearing capacity often fail to meet the experimental requirements for large-span or large-scale structures. Consequently, multi-platform table array systems have received extensive focus in recent years.

Nevertheless, achieving perfect control and coordination between different shaking tables within a multi-table array system remains challenging, making synchronization errors inevitable. Under conditions involving a rigid connection of specimens, synchronization errors between multiple tables generate coupling forces that degrade platform performance and control precision. In severe cases, these errors can trigger overload protection mechanisms and lead to experimental failure[4–6], thereby limiting the application and efficacy of multi-table collaborative testing technologies.

The issues arising from the coupling of a dual-table array via rigid specimens are essentially a dynamic, mutual interaction process between force and position[6]. Under the constraints of a rigid connection, control strategies based purely on position tracking can amplify minute synchronization

 doi:10.20944/preprints202604.1109.v1

errors into substantial coupling forces. This phenomenon may distort the actual motion trajectories transmitted to the specimen and potentially exceed the output capacity limits of the actuators, resulting in the interruption of the test. To address these challenges, traditional control methods have primarily focused on enhancing the control precision of shaking tables under multi-table coupling conditions. For instance, Guan et al. proposed a synchronization control strategy based on a master-slave structure[4]; Li et al. developed a differential movement synchronous tracking control strategy aimed at compensating for the effects of specimen stiffness[5]; Wang et al. introduced a hybrid control strategy combining fuzzy logic control with adaptive inverse control to improve dual-table synchronization and tracking accuracy[7]; and Hu et al. proposed a robust adaptive synchronization and tracking control strategy based on neural networks [8]. However, the core objective of the synchronization control strategies presented in the aforementioned literature is to suppress synchronization errors and enhance tracking performance. Although progress has been made in eliminating coupling forces, most studies prioritize the minimization of displacement synchronization errors or the maximization of control precision without directly accounting for the coupling forces and their dynamic variations induced by inter-table interactions. Given that even minor displacement errors can generate significant coupling forces under rigid connection conditions, there remains considerable room for improvement in existing methods for resolving multi-table coordination issues.

Implementing force control technology to achieve real-time consistency in contact forces between dual platforms is a fundamental approach to resolving multi-table coordination issues. To this end, researchers have proposed compliance control. Compliance control does not refer to a specific algorithm, but rather to a collective term for techniques that regulate the response of a controlled object to external forces and motions through either control-based or mechanical means. Existing compliance control methods are categorized into passive compliance control and active compliance control. Passive compliance control achieves environmental adaptation by installing various highly flexible mechanical devices at the end-effectors[9–11]. While this approach offers the advantages of rapid response and low cost[12], its precision and adaptability are often compromised[13–18].Active compliance control is realized by integrating force feedback with position control, primarily encompassing hybrid force/position control and impedance control. Although hybrid force/position control has been optimized through various methods such as sliding mode control and neural networks, it continues to face challenges, including complex controller design, heavy reliance on environmental modeling, and poor real-time performance[19–23]. In contrast, impedance control regulates the dynamic relationship between force and position by establishing a “mass-damper-spring” model. This allows the system to naturally adapt to environmental interactions, thereby demonstrating significant potential for resolving the aforementioned coupling problems.

Impedance control can be further classified into position-based impedance control and force-based impedance control[24,25]. Position-based impedance control offers the advantage of being easy to implement without requiring an precise dynamic model[26,27]. However, parallel mechanisms, such as multi-degree-of-freedom shaking tables, are characterized by complex dynamic coupling, non-linearity, and anisotropy. Obtaining a precise inverse dynamic model for such systems is difficult, and parameter tuning is complex and demanding, necessitating high system modeling accuracy. Consequently, the direct application of position-based impedance control to parallel mechanisms like shaking tables is significantly constrained. Therefore, to better adapt to the dynamic characteristics of parallel systems and reduce reliance on model precision, force-based impedance control strategies have gained increasing attention for such applications[28,29]. For instance, Haddadin et al. proposed a unified force-impedance control (UFIC) strategy, which aims to integrate the advantages of both impedance control and force control[30]. Bonitz and Hsia introduced a scheme for the impedance control of cooperating manipulators based on internal forces. By enforcing a relationship between velocity and internal force, this approach directly imparts impedance characteristics to the manipulators, achieving simultaneous coordination of motion and internal

 doi:10.20944/preprints202604.1109.v1

forces without prior knowledge of object dynamics, while providing a rigorous proof of system stability[31]. Ba et al. proposed an improved second-order dynamic compliance impedance control system, which significantly enhances control accuracy by rearranging the dynamic compliance composition and incorporating feedforward compensation[32].

However, research regarding impedance control for dual six-degree-of-freedom shaking table arrays remains relatively limited. Only a few studies have preliminarily verified the feasibility of such methods in other parallel systems[33–35], and no specialized impedance control design currently exists for dual-table shaking table systems. For instance, Caccavale et al. proposed a general impedance control scheme for dual-arm robotic systems, combining both centralized and decentralized strategies [36]. Similarly, Ba et al. employed a dual-loop control structure to achieve object-level compliance control and internal load suppression for end-effectors[37].

Based on these discussions, this paper addresses the synchronization control challenges of dual-shaking table array systems under rigid connection conditions by proposing an impedance-based internal force coordination control strategy for dual platforms. First, in Chapter 2, an impedance control strategy targeting real-time equalization of contact forces between the two tables is developed. This strategy generates position compensation values through a second-order discrete impedance filter, seamlessly integrating impedance control into the existing system. This approach effectively suppresses the influence of coupling forces and overcomes the limitations of traditional methods that require pre-defined desired forces. Second, in Chapter 3, the presence of coupling forces and their detrimental effects on control precision and experimental progress are verified by establishing a comprehensive system simulation model, a rigid connection mechanical model, and a method for acquiring table platform forces. Furthermore, the effectiveness of the proposed strategy is validated under various frequency conditions through a combination of Simulink simulations and physical table array experiments.

2. Impedance Control Theory and Internal Force Coordination Control Strategy for Dual-Table Arrays

2.1. Impedance Control Theory

By regulating the dynamic relationship between system position and contact force, force-based impedance control enables the controlled object to achieve compliant motion and precise force tracking under rigid connection conditions. This approach effectively suppresses excessive internal forces caused by motion asynchronization between the two tables. The fundamental principle of this control strategy is illustrated in Figure 1.

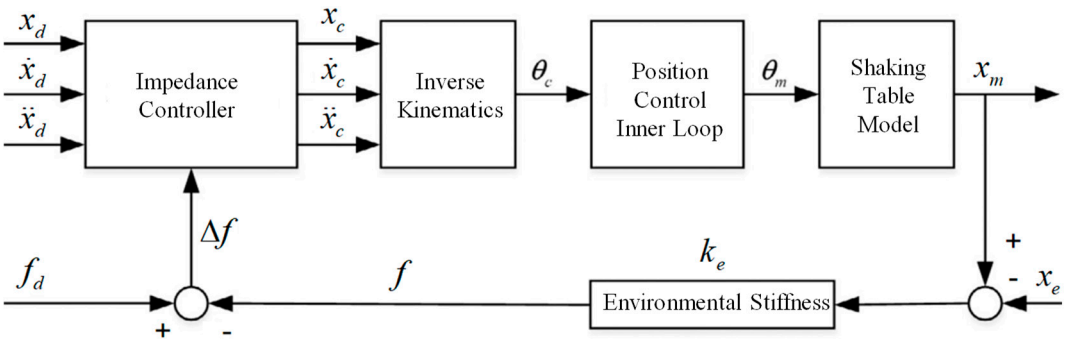

Figure 1. Schematic diagram of impedance control.

In the figure, x_d、$\dot{x}_d$、$\ddot{x}_d$ represent the desired displacement, velocity, and acceleration, respectively; x_c、$\dot{x}_c$、$\ddot{x}_c$ denote the actual output displacement, velocity, and acceleration commands; θ_c and θ_m signify the motor motion angle command and its corresponding actual output value. x_m indicates the actual output displacement of the shaking table, while x_e represents

 doi:10.20944/preprints202604.1109.v1

the external disturbance. k_e denotes the environmental stiffness, then f_d and f represent the desired and actual forces exerted on the platform, respectively.

When the shaking table platform interacts with the external environment, its contact dynamics can be modeled as an equivalent second-order mass-spring-damper system. The equation of motion, representing the impedance model, is defined as follows:

$$M_d(\ddot{x} - \ddot{x}_d) + B_d(\dot{x} - \dot{x}_d) + K_d(x - x_d) = F_{ext} \quad (1)$$

In this equation, M_d is the desired inertia coefficient, which reflects the system's response characteristics to acceleration disturbances; B_d is the desired damping coefficient, which governs system oscillation and energy dissipation; K_d is the desired stiffness coefficient, which determines the system's rigid response degree to external forces; $x, \dot{x}, \ddot{x}$ are the actual displacement, velocity, and acceleration of the platform, respectively; $x_d, \dot{x}_d, \ddot{x}_d$ are the desired displacement, velocity, and acceleration of the platform, respectively; F_{ext} represents the actual contact force between the platform and the specimen.

This model characterizes the relationship between the actual motion and the desired motion. If the system is not in contact with the environment ($F_{ext} = 0$), the platform can accurately track the commanded pose. Once contact occurs, the impedance model dynamically generates position corrections based on the force deviation.

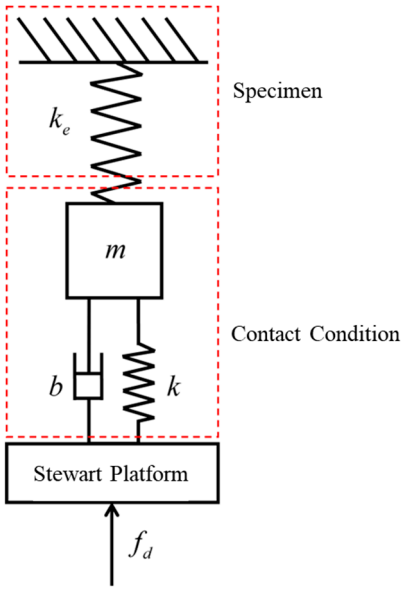

Figure 2. Schematic diagram of the impedance control model decoupling relationships.

To achieve force tracking, the force error $\Delta F = F_d - F_{ext}$ is typically utilized as the input to the impedance model, where F_d denotes the desired contact force. The modified equation of motion is presented in Eq. (2):

$$M_d(\ddot{x} - \ddot{x}_d) + B_d(\dot{x} - \dot{x}_d) + K_d(x - x_d) = \Delta F \quad (2)$$

Assuming the output of the impedance controller is the desired position correction $\Delta x = x - x_d$, and applying the property of the Laplace transform $\mathcal{L}\{\Delta\ddot{x}\} = s^2\Delta X(s)$、$\mathcal{L}\{\Delta\dot{x}\} = s\Delta X(s)$、$\mathcal{L}\{\Delta x\} = \Delta X(s)$、$\mathcal{L}\{\Delta F\} = \Delta F(s)$ (where $\mathcal{L}$ denotes the Laplace transform operator), Eq. (3) is derived from the aforementioned equation as follows:

$$\Delta X(s) = \frac{1}{M_d s^2 + B_d s + K_d} \cdot \Delta F(s) \quad (3)$$

In this equation, s represents the complex frequency variable in the Laplace transform, which converts the differential equation in the time domain (as shown in Eq. 2) into an algebraic relationship

 doi:10.20944/preprints202604.1109.v1

in the frequency domain (as shown in Eq. 3), thereby facilitating system analysis and controller design.

Consequently, the transfer function of the controller is obtained as Eq. (4).

$$G(s) = \frac{\Delta X(s)}{\Delta F(s)} = \frac{1}{M_d s^2 + B_d s + K_d} \tag{4}$$

In the frequency domain, this controller is equivalent to a second-order low-pass filter, where the cut-off frequency and damping ratio are determined by the impedance parameters. To facilitate the implementation of a digital controller, the continuous impedance model must be discretized. By utilizing the bilinear transformation method [38], the discrete-time difference equation is obtained as shown in Eq. (5):

$$\begin{aligned} \Delta x[k] = b_0 \cdot \Delta F[k] + b_1 \cdot \Delta F[k-1] + b_2 \cdot \Delta F[k-2] \\ -a_1 \Delta x[k-1] - a_2 \cdot \Delta x[k-2] \end{aligned} \tag{5}$$

In this equation, $\Delta x[k]$ is the position correction at time step k, $\Delta F[k]$ is the force error at time step k, and a_1, a_2, b_0, b_1, b_2 are the discrete coefficients determined by M_d, B_d, K_d, and the sampling period.

The difference equation can be solved online by utilizing F_{ext} acquired in real-time from force sensors or torque observers. This process generates a corrected position signal setpoint $x_r = x_d + \Delta x$, which is subsequently transmitted to the position controller.

Impedance parameters directly influence system performance and stability. A smaller stiffness coefficient K_d enhances system compliance and reduces contact force, albeit at the cost of diminished position tracking accuracy. An appropriately increased damping coefficient B_d suppresses oscillations and improves stability, whereas excessive damping leads to sluggish system response. The inertia coefficient M_d is typically set near the physical mass of the platform, as a larger value can limit kinetic energy and improve disturbance rejection. To ensure system stability, the impedance parameters must generally satisfy the conditions specified in Eq. (5):

$$B_d > 0, K_d > 0, M_d > \frac{B_d^2}{4K_d} \tag{6}$$

2.2. Impedance-Based Internal Force Coordination Control Strategy for Dual-Shaking Table Arrays

Although impedance control methods demonstrate potential for resolving synchronization issues in dual-table arrays, the application of traditional algorithms is hindered by the difficulty of accurately defining the desired tracking force F_d, which is influenced by multi-dimensional factors such as table kinematics, dynamics, time delays, and control errors. To address these challenges, this study proposes an impedance-based internal force coordination control strategy for dual-shaking table arrays. By coordinating the output forces of both platforms, this strategy effectively suppresses additional coupling forces induced by synchronization errors and enhances system performance and stability. Furthermore, it eliminates the need for pre-defining or calculating a desired force value, thereby ensuring excellent versatility and engineering applicability. The core principle of the proposed strategy is to maintain the contact forces between the two platforms and the specimen at equal magnitudes, thereby eliminating internal force imbalances caused by uncoordinated dual-table motion. The system control structure is illustrated in Figure 3.

Let F_1 and F_2 denote the real-time contact forces between the specimen and platform 1 and platform 2, respectively, which are obtained through force observation on the table platforms. The impedance control law for dual-platform internal force coordination can be designed as follows.

For platform 1, the measured force F_2 from platform 2 is utilized as the desired tracking force for platform 1. This force is then input into its corresponding impedance controller (a second-order discrete filter) to calculate the displacement correction increment Δx_1:

$$\Delta x_1 = G_1(s) \cdot (F_2 - F_1) \tag{7}$$

 doi:10.20944/preprints202604.1109.v1

In the equation, $Z_1(s)$ denotes the transfer function of the impedance controller for platform 1.

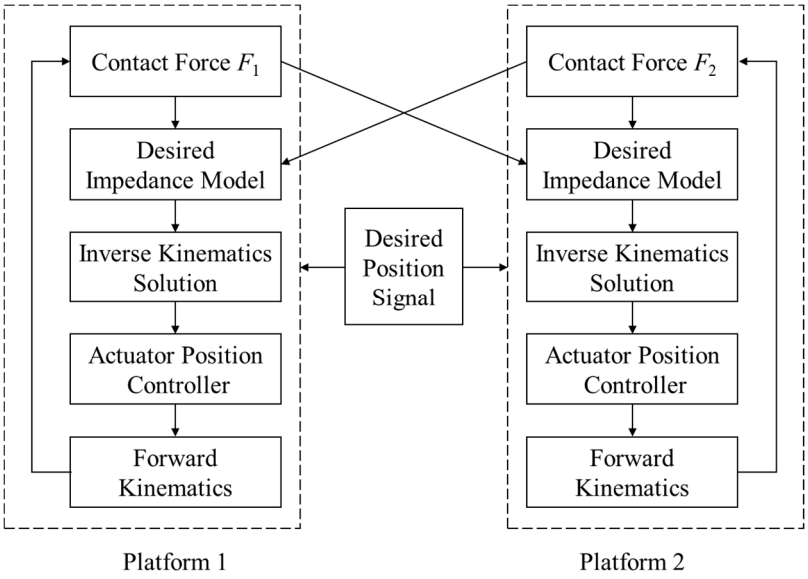

Figure 3. Impedance-based internal force coordination control strategy flowchart.

Similarly, the measured contact force F_1 of platform 1 is utilized as the desired tracking force for platform 2. This value is input into its respective impedance controller to calculate the displacement correction increment Δx_2:

$$\Delta x_2 = G_2(s) \cdot (F_1 - F_2) \tag{8}$$

In the equation, $Z_2(s)$ denotes the transfer function of the impedance controller for platform 2.

By adding displacement corrections to the original trajectories x_{d1} and x_{d2}, new tracking commands are generated according to Eq. (9). These are then converted into actuator commands through inverse kinematics for position servo control.

$$\begin{aligned} x_{r1} &= x_{d1} + \Delta x_1 \\ x_{r2} &= x_{d2} + \Delta x_2 \end{aligned} \tag{9}$$

In these two equations, x_{d1} and x_{d2} represent the original reference displacements for platform 1 and platform 2, respectively. Δx_1 and Δx_2 denote the displacement correction increments derived from the impedance control for platform 1 and platform 2. x_{r1} and x_{r2} are the corrected reference displacement commands for platform 1 and platform 2.

This strategy utilizes the force information from the dual-table array as a mutual control objective, thereby eliminating the need for pre-defined desired force values and avoiding the challenge of accurately specifying F_d in traditional impedance control. Simultaneously, by directly suppressing internal force coupling through force equilibrium, this approach is applicable to various specimen masses, connection stiffnesses, and motion trajectories, enhancing both system synchronization precision and stability.

3. Problem Analysis and Experimental Validation of the Dual-Table Array System

To investigate the synchronization control challenges of dual-table array systems under rigid connection conditions, it is essential to first establish an accurate system dynamic model and analyze the underlying coupling mechanisms. Taking the Stewart platform dual-table array system as an example, this section constructs a comprehensive mechanical model incorporating both platform dynamics and rigid connection characteristics. This model is utilized to verify the impact of coupling

 doi:10.20944/preprints202604.1109.v1

forces, induced by synchronization errors between the two tables, on system dynamic performance and synchronization precision. Furthermore, this section examines the effectiveness of the proposed impedance-based internal force coordination control strategy for dual-shaking table arrays.

3.1. System Modeling and Coupling Error Analysis for Dual-Table Arrays

3.1.1. Stewart Platform Modeling

The Stewart platform is constructed from six independent legs, each utilizing a servo-electric cylinder system as the primary actuator. Within each leg, the electric cylinder converts the rotational motion of the motor into linear thrust. This conversion process adheres to the principle of energy conservation while accounting for transmission efficiency losses. Based on this, the relationship between the output force of a single-leg electric cylinder and the motor torque can be derived as follows:

$$T_e = \frac{F \cdot h}{2\pi\eta} \qquad (10)$$

In the equation, denotes the lead of the ball screw, and represents the transmission efficiency of the screw.

The electromagnetic torque T_e produced by the servo motor acts upon the ball screw to generate a tangential force F_t. The relationship between the torque and the tangential force is expressed as Eq. (11):

$$F_t = \frac{T_e}{r} \qquad (11)$$

In this equation, r represents the radius of the ball screw.

The work performed by the motor during one full revolution is $F_t \times 2\pi r$. Converting this work into the linear thrust F_{leg} required to move the load by one lead h, and accounting for the transmission efficiency η, the mechanical work balance of the ball screw is given by Eq. (12):

$$F_t \times 2\pi r \times \eta = F_{leg} \times h \qquad (12)$$

Substituting Eq. (11) into Eq. (12) and solving for F_{leg} yields the theoretical conversion formula:

$$F_{leg} = \frac{2\pi r\eta}{h} \times \frac{T_e}{r} = \frac{2\pi\eta T_e}{h} \qquad (13)$$

In practical applications, to facilitate unit conversion (e.g., h is commonly expressed in mm/r, while T_e is in N·m) and to compensate for unmodeled dynamic losses, an empirical conversion coefficient $K = 5.338$, obtained through iterative testing and calibration, is introduced. The final engineering formula adopted is:

$$F_{leg} = \frac{2\pi\eta T_e}{h} \times 5.338 \qquad (14)$$

Subsequently, the vertical (Z-axis) force synthesis for the table platform is performed. Based on the principles of statics, the thrust force from each individual leg is projected onto the Z-axis of the table platform and aggregated. Simultaneously, the inertial force of the platform is compensated. The geometric relationships for this six-axis force synthesis are illustrated in Figure 4.

The direction of the thrust F_{leg} for a single leg is aligned with its longitudinal axis. The component of this force in the vertical direction (Z-axis) of the platform, denoted as $F_{z,leg}$, is expressed as:

$$F_{z,leg} = F_{leg} \cdot \sin\theta = F_{leg} \cdot \frac{Z_{platform}}{L_{leg}} \qquad (15)$$

 doi:10.20944/preprints202604.1109.v1

In this equation, θ represents the inclination angle between the leg and the horizontal plane, $Z_{platform}$ is the current height of the moving platform, and Z_{leg} denotes the real-time length of the leg.

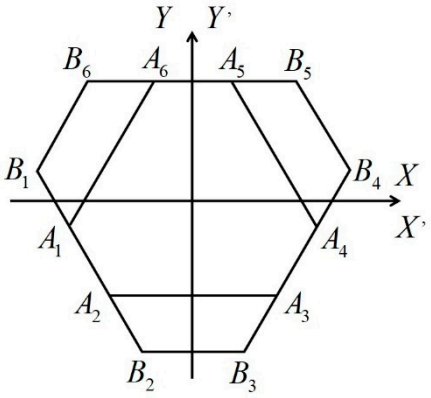

Figure 4. Top view of the Stewart platform mechanism.

The total Z-axis force $F_{z,total}$ exerted on the platform is the summation of the Z-axis components from all six legs, adjusted by subtracting the inertial force generated by the platform mass $m_{platform}$ undergoing Z-axis acceleration a_z:

$$F_{z,total} = \sum_{i=1}^{6} F_{z,leg_i} - m_{platform} \cdot a_z \qquad (16)$$

This calculation yields the net contact force between the platform and the specimen.

3.1.2. Mechanical Models for Rigid Connections

The mechanical model of the rigid connection for the dual-shaking table array system can be represented as an equivalent spring-mass model, as illustrated in Figure 5.In this model, M_s and M_t denote the mass of the specimen and the table platform, respectively. F_1 and F_2 represent the actuation forces of platform 1 and platform 2, while x_1 and x_2 signify the displacements of their respective platforms. x_s represents the displacement of the center of the specimen. Under the assumption of perfect rigid connection and homogeneity, it can be considered that $x_s = \frac{(x_1+x_2)}{2}$. The parameters k and c denote the stiffness coefficient and damping coefficient of the connection between the platform and the specimen, respectively. Although these values are negligible compared to the structural stiffness and damping in the case of a perfectly rigid connection, they cannot be entirely ignored, particularly when performing high-frequency vibration simulations.

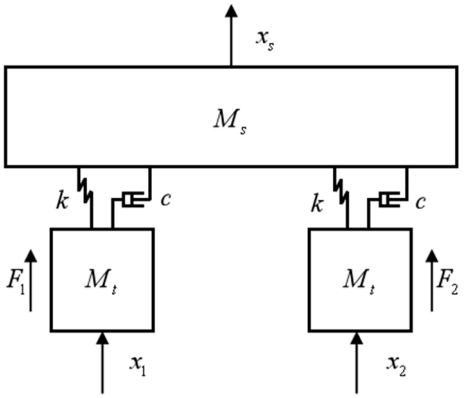

Figure 5. Rigid connection mechanical model of the dual-table array.

 doi:10.20944/preprints202604.1109.v1

The force equilibrium equations for the dual-table array system with a specimen are as follows.

$$\begin{cases} M_t s^2 x_1 = F_1 - (cs + k)(x_1 - x_s) - \dfrac{M_s g}{2} \\ M_t s^2 x_2 = F_2 - (cs + k)(x_2 - x_s) - \dfrac{M_s g}{2} \end{cases} \tag{17}$$

In these equations, s denotes the Laplace operator, which acts as a differential operator in the complex frequency domain. Specifically, s corresponds to the velocity $\dot{x}(t)$ in the time domain, representing the platform velocity response, while s^2 corresponds to the acceleration $\ddot{x}(t)$, representing the platform acceleration response. In dynamic system analysis, applying the Laplace transform to convert time-domain differential equations into algebraic equations in the complex frequency domain significantly simplifies the analysis of system dynamic characteristics and controller design.

By substituting $x_s = \frac{(x_1+x_2)}{2}$ into Eq. (17) and rearranging, the system equations of motion are derived as follows:

$$\begin{cases} M_t s^2 x_1 = F_1 - (cs + k)\dfrac{(x_1 - x_2)}{2} - \dfrac{M_s g}{2} \\ M_t s^2 x_2 = F_2 - (cs + k)\dfrac{(x_2 - x_1)}{2} - \dfrac{M_s g}{2} \end{cases} \tag{18}$$

Equation (18) is derived by rearranging the aforementioned expressions:

$$\begin{cases} s^2 x_1 = \dfrac{F_1 + (cs + k)\frac{x_2}{2} - \frac{M_s g}{2}}{M_t + \frac{cs + k}{2s^2}} \\ s^2 x_2 = \dfrac{F_2 + (cs + k)\frac{x_1}{2} - \frac{M_s g}{2}}{M_t + \frac{cs + k}{2s^2}} \end{cases} \tag{19}$$

In these equations, $s^2 x_1$ represents the table platform acceleration response of platform 1, while $s^2 x_2$ represents the table platform acceleration response of platform 2.

This mechanical model elucidates the dynamic coupling mechanism of the dual-table array system under rigid connection conditions, establishing a theoretical foundation for the subsequent development of the system simulation model and the analysis of its dynamic response characteristics.

3.1.3. Analysis of Synchronization Errors and Coupling Forces

To investigate the dynamic characteristics of the dual-shaking table array system under rigid connection conditions and to validate the existence and impact of coupling forces, this section conducts a comprehensive study of the system response under sinusoidal excitation with varying frequencies and amplitudes, integrating both simulation analysis and experimental testing.

Based on the previously established Stewart platform system model and the mechanical model for the dual-table array with rigid connection, four typical sinusoidal displacement signal scenarios are selected for simulation analysis. The selection of experimental conditions strictly adheres to the effective operating frequency range of the Stewart platform (0.1–10 Hz) to ensure the validity and comparability of the system response. The amplitude settings for each working condition are determined according to the frequency-amplitude envelope commonly utilized in engineering practice; specifically, the displacement amplitude is decreased as the frequency increases within the feasible motion range of the platform to generate a series of test conditions with equivalent dynamic intensity. The selected frequencies are 2 Hz, 3 Hz, 4 Hz, and 5 Hz, with corresponding amplitudes of 40 mm, 20 mm, 13 mm, and 8 mm, respectively.

Without the implementation of impedance control, the control algorithm used in the control experiments is the native PID control algorithm of the Stewart platform. Within the simulation model,

 doi:10.20944/preprints202604.1109.v1

a leg force exceeding 6 kN is defined as the safety limit to simulate the termination condition in actual experimental tests.

To better evaluate the control performance of the Stewart platform dual-table array system, this study introduces three performance assessment metrics: time delay, root mean square error (RMSE), and peak error between the reference input r and the actual output y. These metrics enable a multi-dimensional quantitative analysis of simulation and experimental data from three distinct perspectives: dynamic response, steady-state precision, and extreme deviation. The details of these three indicators are summarized in Table 1.

Table 1. Performance evaluation metrics for the Stewart platform.

Evaluation Metric	Formula	Unit
Time Delay（J_1）	$J_1 = \underset{k}{argmax}\left[\sum_{1} y_n^{(1)}(i)x_m(i-k)\right]^{-1}$	ms
Root Mean Square Error (RMSE)（J_2）	$J_2 = \sqrt{\frac{\sum_{i=1}^{N}\left[x_m(i)-y_n^{(1)}(i)\right]^2}{\sum_{i=1}^{N}\left[y_n^{(1)}(i)\right]^2}} \times 100$	%
Peak Error（J_3）	$J_3 = \frac{max\left\|x_m(i)-y_n^{(1)}(i)\right\|}{max\left\|y_n^{(1)}(i)\right\|} \times 100$	%

The simulation results demonstrate that under all tested working conditions, the peak contact force between platform 2 and the specimen exceeds the maximum allowable load of 6 kN. The peak contact force exhibits a positive correlation with the excitation frequency, as detailed in Table 2.

Table 2. Comparison of peak contact force on platform 2 between simulation and experiment.

Test Condition	Simulation Peak Force (N)	Experimental Peak Force (N)	Relative Error (%)
2 Hz, 40 mm	6597	6503	1.45
3 Hz, 20 mm	6787	6705	1.22
4 Hz, 13 mm	7086	7185	1.38
5 Hz, 8 mm	7241	7051	2.69

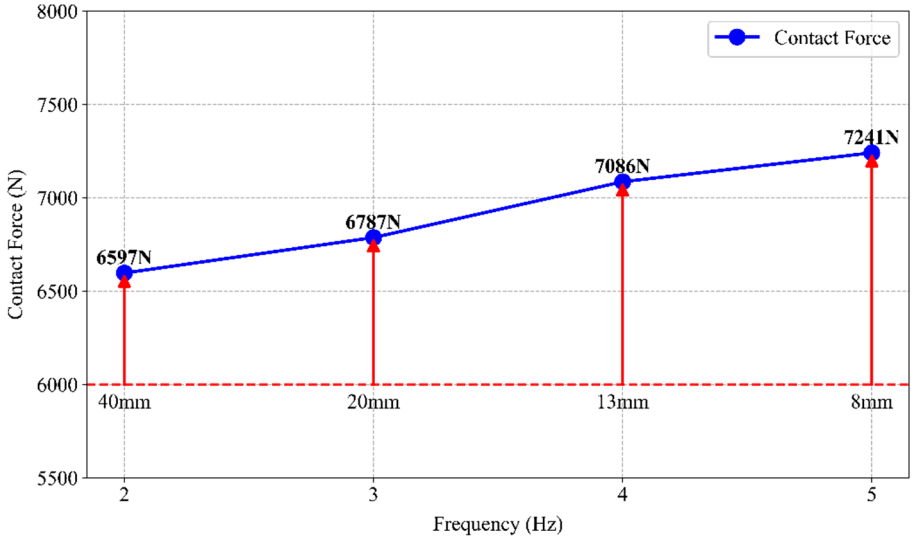

Figure 6. Peak contact force on platform 2 under simulation working conditions.

 doi:10.20944/preprints202604.1109.v1

Furthermore, the displacement reproduction accuracy decreases significantly as the frequency increases. As shown in Table 3, the root mean square error (RMSE) for platform 1 and platform 2 increases from 3.23% and 3.31% at 2 Hz to 14.03% and 14.53% at 5 Hz, respectively, indicating a substantial degradation in performance. Although the peak error remains relatively stable, ranging between 1.1% and 1.3%, the higher inertial forces generated during high-frequency motion imply that even smaller error magnitudes can trigger a system overload alarm.

Table 3. Simulation results of displacement reproduction for the dual-shaking table array.

Test Condition (Freq/Amp)	Category	RMSE (%)	Peak Error (%)
2Hz/40mm	Platform 1 Reproduction	3.23	1.29
	Platform 2 Reproduction	3.31	1.32
	Dual-Table Synchronization	0.08	0.03
3Hz/20mm	Platform 1 Reproduction	6.55	1.31
	Platform 2 Reproduction	6.70	1.34
	Dual-Table Synchronization	0.16	0.03
4Hz/13mm	Platform 1 Reproduction	10.19	1.33
	Platform 2 Reproduction	10.42	1.36
	Dual-Table Synchronization	0.26	0.03
5Hz/8mm	Platform 1 Reproduction	14.03	1.12
	Platform 2 Reproduction	14.53	1.16
	Dual-Table Synchronization	0.58	0.04

It should be noted that the actual output force of the platform can exceed the maximum allowable load to a certain extent. Furthermore, the measurement range of the force instrumentation is capable of recording forces exceeding this limit. Therefore, peak contact forces greater than 6 kN may occur in practice. However, the control precision and operational stability of the platform cannot be effectively guaranteed under such conditions. Consequently, 6 kN is adopted as the termination threshold for both experimental and simulation studies in this research.

The simulation results indicate that the dynamic response capability of the controller degrades when the sum of the inertial forces and the coupling forces between the two platforms consistently approaches or exceeds the load limit. Meanwhile, dynamic coupling forces generated by uncoordinated dual-table motion may significantly exceed the maximum allowable load of the platform. This is especially evident under high-frequency conditions and often leads to the termination of simulations or experiments. Such forces further exacerbate the tracking deviation of the system and exert a negative influence on the synchronization precision.

Subsequently, based on the simulation results of the dual-table array system, corresponding experimental verification is performed on the Stewart platform dual-table array system. The rigid specimen selected for the experiment is a 20a I-beam, designed and fabricated in accordance with the GB/T 706-2016 standard. The I-beam is connected to the Stewart platform tables using steel plates to ensure a rigid connection. Additionally, appropriate supplementary masses are incorporated based on similarity design principles, as illustrated in Figure 7.

 doi:10.20944/preprints202604.1109.v1

Figure 7. Synchronous vibration test setup for the rigid-connected dual-table array. **(a)** Dual-table array loading test system **(b)** Single table load and connection configuration.

The experimental setup utilizes the same sinusoidal displacement signals as the simulation. We observed the contact force between the platforms and the specimen during the displacement reproduction process. We also evaluated the individual displacement reproduction accuracy of each platform and the overall synchronization performance of the dual-table array. The results indicate that the peak contact force between platform 2 and the specimen is significantly high during the experiment. This high contact force triggers the overload protection mechanism， and this condition is shown in Figure 8.

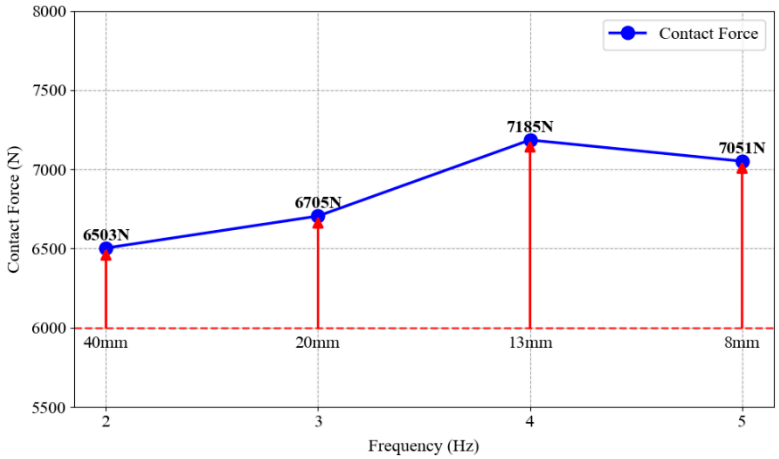

Figure 8. Experimental peak contact force on platform 2.

Experiments demonstrate that the time delay of the dual-table array system remains at approximately 0.01 s. However, the system shows a significant degradation in displacement reproduction accuracy. The root mean square error of displacement tracking reaches 15.29% to 31.93%. The peak error ranges from 2.65% to 6.56%. The absolute value of the displacement synchronization error between the two platforms is small. The root mean square error does not exceed 0.68%, and the peak error does not exceed 0.2%. However, the dynamic coupling force effect is substantial due to the high structural stiffness of the components. These results are detailed in Table 4.

Table 4. Displacement reproduction accuracy comparison between the rigid-connected dual-shaking table array and a single Stewart platform.

Test Condition (Freq/Amp)	System Type	Time Delay (s)	RMSE (%)	Peak Error (%)
2 Hz / 40 mm	Single Stewart Platform	0.01	14.82	6.48

 doi:10.20944/preprints202604.1109.v1

	Dual-table Array (Platform 1)	0.01	15.29	6.56
	Dual-table Array (Platform 2)	0.01	15.27	6.51
	Dual-table Synchronization Status	0	0.22	0.19
	Single Stewart Platform	0.01	20.99	4.45
	Dual-table Array (Platform 1)	0.01	22.02	4.61
3 Hz / 20 mm	Dual-table Array (Platform 2)	0.01	21.98	4.65
	Dual-table Synchronization Status	0	0.326	0.12
	Single Stewart Platform	0.01	26.25	3.57
	Dual-table Array (Platform 1)	0.01	27.22	3.74
4 Hz / 13 mm	Dual-table Array (Platform 2)	0.01	27.22	3.76
	Dual-table Synchronization Status	0	0.49	0.13
	Single Stewart Platform	0.01	30.64	2.60
	Dual-table Array (Platform 1)	0.01	31.93	2.65
5 Hz / 8 mm	Dual-table Array (Platform 2)	0.01	31.90	2.66
	Dual-table Synchronization Status	0	0.68	0.08

Simulation and experimental results demonstrate that under rigid connection conditions, even minor synchronization errors are converted into substantial additional internal forces due to motion constraints. These internal forces not only cause instantaneous platform overloading and trigger protection mechanisms but also significantly degrade both tracking and synchronization accuracy.

3.2. Simulation Validation and Analysis

To validate the effectiveness of the impedance-based internal force coordination control strategy, this section conducts synchronized vibration simulation research based on the rigid connection model established in Section 3.1.2. The simulation incorporates dual-platform interactive force coordination impedance control. The testing frequencies and amplitudes are identical to those in the previous experiments, covering the following four sinusoidal displacement signal working conditions: Working Condition 1: 2 Hz, 40 mm; Working Condition 2: 3 Hz, 20 mm; Working Condition 3: 4 Hz, 13 mm; Working Condition 4: 5 Hz, 8 mm.

The impedance controller in the simulation utilizes the second-order discrete filter form mentioned previously. Its continuous-domain model is defined as:

$$Z(s) = \frac{1}{M_d s^2 + B_d s + K_d} \tag{20}$$

In this equation, the inertia coefficient M_d is set to 340 kg, corresponding to the actual payload mass of the platform, to enhance system stability. The damping coefficient B_d is set between 4,600 and 4,800. To balance force control precision with stability, the stiffness coefficient K_d is designed to decrease as the frequency increases, transitioning gradually from 800 to 590.

The simulation results demonstrate that the proposed impedance-based internal force coordination control strategy effectively reduces the contact force between the platform and the specimen across different frequencies, maintaining it below the maximum allowable load of the platform. Taking the sinusoidal working condition with a frequency of 5 Hz and an amplitude of 8 mm as an example, once the contact force stabilizes, the average peak values for platform 1 and platform 2 are 5669 N and 5688 N, respectively, resulting in a force discrepancy of 19 N between the two tables. Regarding displacement reproduction, the dual-table synchronization root mean square error (RMSE) is 2.89%, and the peak error is 0.20%, indicating high tracking precision. These results are illustrated in Figure 9, Figure 10, and Table 5.

 doi:10.20944/preprints202604.1109.v1

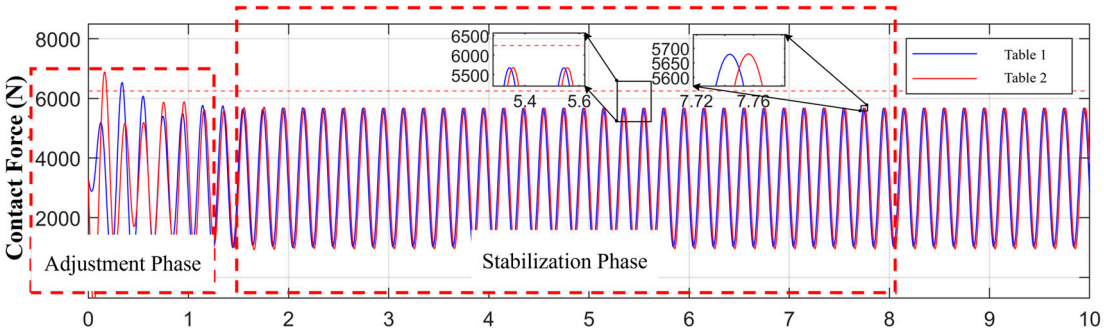

Figure 9. Platform-specimen contact forces under impedance-based internal force coordination control in simulation.

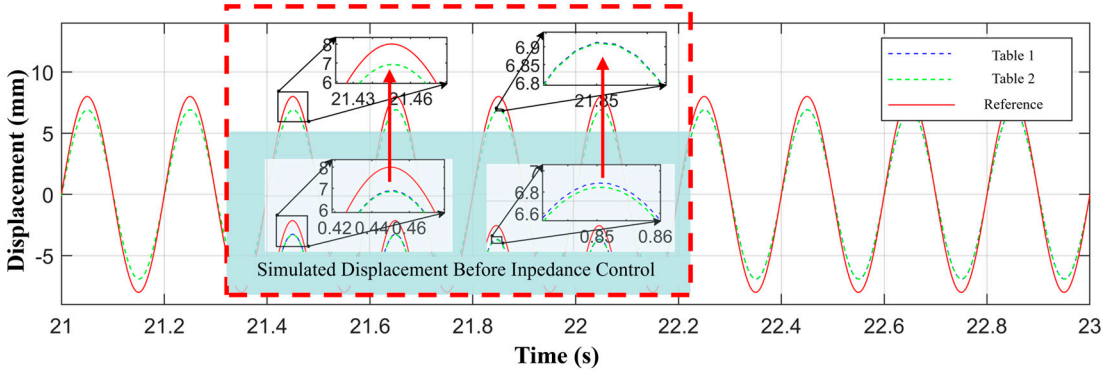

Figure 10. Displacement reproduction under impedance-based internal force coordination control in simulation.

As the frequency increases, the proposed control strategy maintains robust performance by dynamically adjusting impedance parameters, specifically by reducing the stiffness coefficient and optimizing the damping coefficient. At 3 Hz, the force discrepancy between the two tables is 18 N; at 4 Hz, it is 9 N; and at 5 Hz, it is 19 N. Furthermore, the displacement reproduction errors remain within acceptable limits across all tested frequencies.

Compared to the baseline data obtained prior to the implementation of the proposed strategy, as detailed in Table 5, the peak contact force on platform 2 decreases significantly under all working conditions following the application of the force control. This evidence confirms that the proposed impedance-based internal force coordination control strategy effectively eliminates the additional forces induced by synchronization errors under rigid connection conditions.

Table 5. Comparison of dual-table interaction forces before and after impedance control in simulation.

Test Condition (Freq/Amp)	Controlled Platform 1 Force (N)	Controlled Platform 2 Force (N)	Uncontrolled Platform 2 Force (N)	Uncontrolled Force Discrepancy (N)	Controlled Force Discrepancy (N)
2 Hz/40 mm	5419	5427	6597	1170	8
3 Hz/20 mm	5629	5647	6787	1140	18

 doi:10.20944/preprints202604.1109.v1

4 Hz/13 mm	5842	5851	7086	1235	9
5 Hz/8 mm	5669	5688	7241	1553	19

The simulation data for the dual-shaking table array system after applying the proposed strategy are presented in Table 6. A comparison between these results and the simulation data from the dual-shaking table array system without the implementation of this strategy indicates that the proposed control scheme enhances both the displacement reproduction accuracy and the synchronization control precision of the Stewart platform dual-shaking table array system. Consequently, the simulation results demonstrate the effectiveness of the Impedance-based internal force coordination control strategy for dual-shaking table arrays in addressing the challenges associated with rigid specimens under rigid connection conditions.

Table 6. Simulation results of displacement reproduction for the dual-shaking table array under impedance control.

Test Condition (Freq/Amp)	Category	RMSE (%)	Peak Error (%)
2 Hz/40 mm	Platform 1 Reproduction	3.16	1.26
	Platform 2 Reproduction	3.16	1.26
	Dual-Table Synchronization	0.002	0.001
3 Hz/20 mm	Platform 1 Reproduction	6.34	1.27
	Platform 2 Reproduction	6.35	1.27
	Dual-Table Synchronization	0.01	0.002
4 Hz/13 mm	Platform 1 Reproduction	9.90	1.288
	Platform 2 Reproduction	9.91	1.29
	Dual-Table Synchronization	0.01	0.001
5 Hz/8 mm	Platform 1 Reproduction	13.51	1.08
	Platform 2 Reproduction	13.54	1.08
	Dual-Table Synchronization	0.03	0.002

3.3. Experimental Validation and Analysis

To validate the effectiveness of the Impedance-based internal force coordination control strategy for dual-shaking table arrays in a practical system, this section presents the results of synchronous vibration experiments. These experiments are compared with test cases where the strategy was not applied. The experiments utilize the same four sinusoidal displacement signal working conditions as established in Chapter 3 (2 Hz–40 mm, 3 Hz–20 mm, 4 Hz–13 mm, and 5 Hz–8 mm). As shown in Table 7, after implementing the Impedance-based internal force coordination control strategy for dual-shaking table arrays, the system successfully avoids the protection alarms previously triggered by platform 2 overloading. The dual-shaking table array system operates stably and completes tests under all working conditions.

Regarding contact force control, the peak contact force of platform 2 at all frequencies decreases significantly following the application of the control strategy, with an average reduction of 15.09%. These values remain below the maximum allowable load of the platform. Although the force discrepancy between the two shaking tables increases slightly with frequency, the force control strategy effectively suppresses the coupling forces induced by the rigid connection, ensuring the continuity of the experiment.

 doi:10.20944/preprints202604.1109.v1

It should be noted that the force discrepancy between the two shaking tables is higher in the physical experiments than in the simulation working conditions. This is attributed to factors such as model errors, parameter uncertainties, sensor noise, time-delay effects, and unmodeled nonlinear dynamics (e.g., friction and backlash) that are not fully captured in the idealized simulation model. Future research will explore the use of adaptive impedance control, robust control strategies, or multi-sensor information fusion technologies to further improve the robustness and control precision of the system[39–41].

Table 7. Experimental contact force comparison before and after impedance control.

Test Condition (Freq/Amp)	Controlled Platform 1 Force (N)	Controlled Platform 2 Force (N)	Uncontrolled Platform 1 Force (N)	Platform 2 Force Reduction (N)	Dual-Table Force Discrepancy (N)	Platform 2 Reduction Percentage (%)
2 Hz/40 mm	5405	5462	6503	1041	57	16.01%
3 Hz/20 mm	5509	5719	6705	986	210	14.71%
4 Hz/13 mm	5709	6037	7185	1148	328	15.98%
5 Hz/8 mm	5391	6087	7051	964	696	13.67%

Regarding displacement synchronization accuracy, the system performance improves significantly after implementing the Impedance-based internal force coordination control strategy for dual-shaking table arrays. The root mean square error of dual-table synchronization decreases from 0.22% to 0.03% at 2 Hz, from 0.32% to 0.05% at 3 Hz, from 0.49% to 0.13% at 4 Hz, and from 0.68% to 0.29% at 5 Hz. As illustrated in Figure 11, the consistency of the displacement output between the two platforms improves markedly, which validates the effectiveness of the control strategy in enhancing synchronization precision.

Table 8. Experimental results of displacement reproduction for the dual-shaking table array under impedance control.

Test Condition (Freq/Amp)	Category	Time Delay (s)	RMSE (%)	Peak Error (%)
2 Hz/40 mm	Platform 1 Reproduction	0.01	14.99	6.15
	Platform 2 Reproduction	0.01	14.99	6.16
	Dual-Table Synchronization	0	0.03	0.01
3 Hz/20 mm	Platform 1 Reproduction	0.01	21.99	4.52
	Platform 2 Reproduction	0.01	21.97	4.54
	Dual-Table Synchronization	0	0.05	0.01
4 Hz/13 mm	Platform 1 Reproduction	0.01	27.16	3.72
	Platform 2 Reproduction	0.01	27.19	3.72
	Dual-Table Synchronization	0	0.13	0.03

 doi:10.20944/preprints202604.1109.v1

5 Hz/8 mm	Platform 1 Reproduction	0.01	31.86	2.64
	Platform 2 Reproduction	0.01	31.87	2.65
	Dual-Table Synchronization	0	0.29	0.03

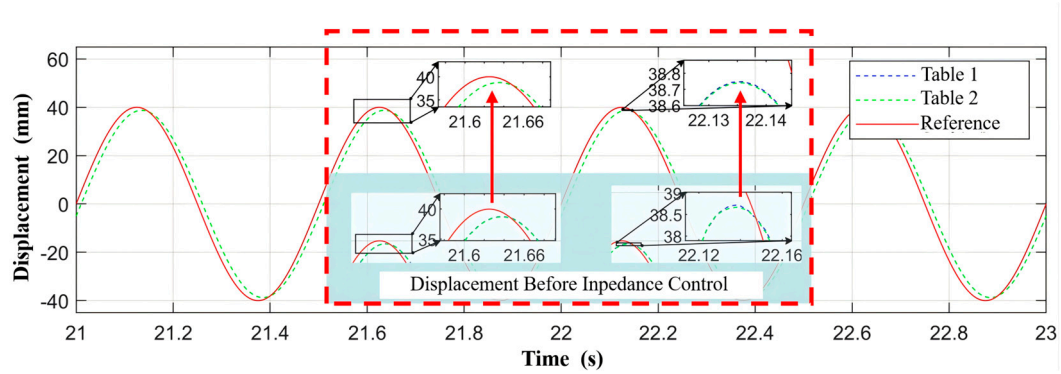

2 Hz/40 mm

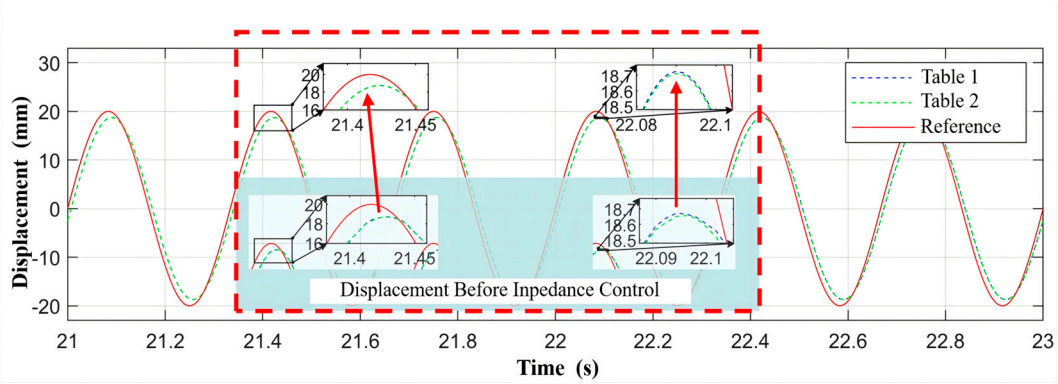

3 Hz/20 mm

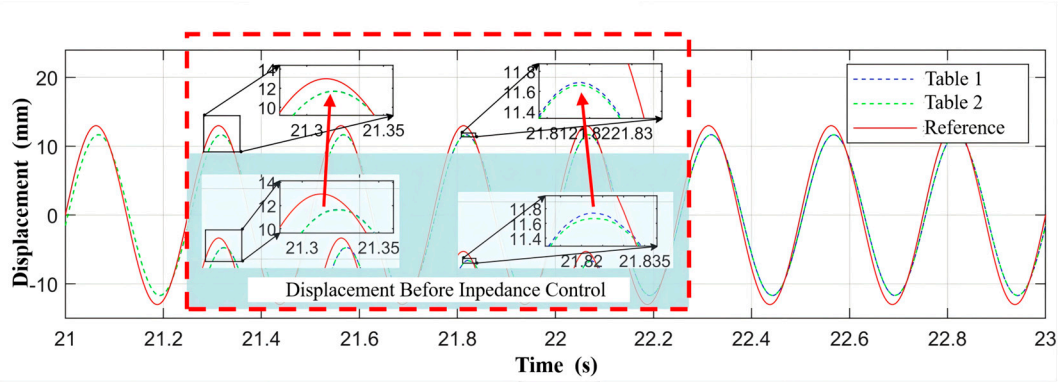

4 Hz/13 mm

 doi:10.20944/preprints202604.1109.v1

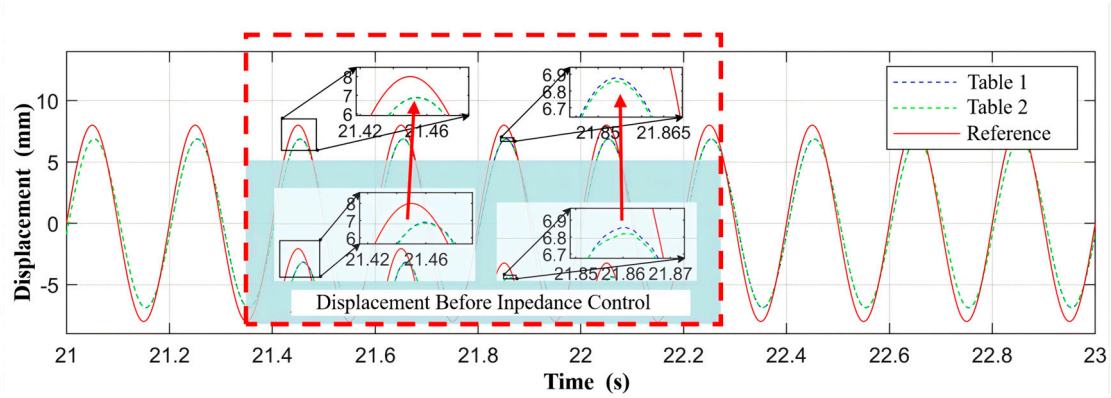

5 Hz/8 mm

Figure 11. Displacement synchronization curves before and after impedance-based internal force coordination control.

4. Discussions

The experimental and numerical investigations conducted in this study confirm that an impedance-driven force coordination framework can effectively neutralize the destabilizing coupling effects inherent in rigidly connected dual-shaking table configurations. By dynamically balancing inter-platform interaction loads through mutual force feedback and a discrete impedance filter, the proposed control architecture successfully prevents actuator saturation while simultaneously enhancing trajectory tracking fidelity and inter-table synchronization across the tested frequency spectrum. These outcomes validate the initial working hypothesis that treating multi-table synchronization as a dynamic force-position interaction problem, rather than a purely kinematic tracking task, yields superior robustness under rigid constraint conditions.

Interpreting these results in light of prior research reveals a clear methodological shift. Conventional multi-table control architectures have predominantly prioritized displacement error minimization, frequently employing master-slave hierarchies, differential tracking schemes, or data-driven compensators. While such approaches improve kinematic alignment, they often overlook how minute positional mismatches are rapidly amplified into substantial internal loads when rigid specimens couple the platforms. Hybrid force/position strategies and passive compliance devices have been explored as alternatives, yet they typically demand intricate controller tuning, heavy reliance on accurate environmental models, or exhibit limited adaptability to varying payload characteristics. In contrast, the present methodology circumvents the need for predefined force setpoints, which are notoriously difficult to estimate accurately due to system nonlinearities, time delays, and shifting dynamic loads. By allowing each platform to adaptively reference the other's measured contact force, the controller inherently suppresses load imbalances without requiring complex inverse dynamics or extensive parameter identification. This design philosophy not only simplifies implementation but also enhances the system's resilience to model uncertainties.

The broader implications of these findings are substantial for structural engineering and seismic testing practices. The demonstrated capacity to maintain stable operation under rigid specimen configurations significantly expands the experimental envelope for large-scale or multi-component structural systems that exceed the capacity of single-table facilities. The substantial reduction in inter-platform force discrepancies observed in physical trials directly translates to improved data reliability, extended equipment service life, and a markedly lower risk of premature test termination due to overload protection triggers. Moreover, the model-agnostic nature of the control architecture facilitates straightforward integration into existing shaking table infrastructure, lowering the technical and financial barriers for widespread adoption in academic and industrial testing centers.

Despite these advancements, certain limitations must be acknowledged. Physical experiments consistently exhibited marginally higher force deviations compared to numerical simulations. This discrepancy is attributable to real-world nonlinearities that were idealized in the simulation

 doi:10.20944/preprints202604.1109.v1

environment, including joint friction, mechanical backlash, sensor measurement noise, communication latency, and parameter drift under prolonged operation. Additionally, the current implementation relies on a pre-scheduled adjustment of impedance coefficients across different frequency bands. While effective for steady-state sinusoidal excitations, this approach may require further refinement to handle highly transient or broadband seismic waveforms without manual intervention.

Future research should therefore focus on embedding adaptive or learning-based mechanisms to autonomously tune impedance parameters in real time, thereby enhancing robustness against environmental uncertainties and payload variations. Integrating multi-sensor data fusion techniques could further mitigate measurement noise and compensate for time-delay effects in force estimation. Expanding the framework to accommodate three or more synchronized tables, as well as validating performance under complex multi-axial earthquake records and varying specimen stiffness conditions, would provide a more comprehensive evaluation of its scalability and industrial readiness. Finally, exploring the integration of digital twin technologies for predictive load management and self-optimizing control could pave the way for fully autonomous, high-fidelity multi-table testing environments. Overall, by shifting the control paradigm from rigid position tracking to adaptive force equilibrium, the proposed strategy offers a pragmatic and effective solution to a longstanding challenge in collaborative seismic testing, opening new avenues for large-scale structural evaluation.

5. Conclusions

This study addresses the coupling force problem in Stewart platform dual-shaking table array systems under rigid connection conditions. An impedance-based internal force coordination control strategy is proposed, and its effectiveness is validated through system simulation and experimental research. The primary conclusions are as follows:

1. An impedance-based internal force coordination control strategy for dual-shaking table arrays is developed. This method utilizes the measured contact forces of the two platforms as the target forces for each other. It employs a second-order discrete impedance filter to generate displacement corrections and achieves dynamic equilibrium of internal forces between the tables. Unlike traditional impedance control, this method eliminates the need for preset target forces. This approach avoids control deviations caused by inaccurate force settings and offers strong adaptability and engineering practicality.
2. A synchronous vibration simulation model for the Stewart platform dual-shaking table array system under rigid connection is established. This model reveals the mechanism behind the system issues caused by rigid specimens, providing a reliable basis for controller design.
3. Simulation and experimental results demonstrate that the proposed control strategy effectively suppresses coupling forces and significantly improves system performance. In simulation, the force discrepancy between table platforms is reduced by an average of 95.39%. In physical experiments, the dual-table synchronization error is reduced by an average of 76.1%, with a maximum reduction of 86.2%. The strategy maintains platform force within safety thresholds to avoid overload-induced interruptions. It also enhances displacement reproduction accuracy and synchronization control stability.

Funding: This study is supported by the following funding: Science and Technology Research and Development Program Project of China railway group limited (2025-Special-04), Natural Science Foundation of China (U2368210), Fundamental Research Project of China Railway Group (L2024G015(T001)).

Data Availability Statement: The data used to support the findings of this study are available from the corresponding author on request.

Conflicts of Interest: The authors declare no conflicts of interest.

 doi:10.20944/preprints202604.1109.v1

References

1. Zhao F., Yu S.B., Li B., et al. Research Advances on Large-Scale Shaking Table Test for Rock Slopes under Earthquake. Earth Sci. 2022, 47, 4498–4512.
2. Ding Y., Dong Y.Q., Shi Y.D. State-of-the-Art on Seismic Isolation of Long-Span Spatial Structures. J. Southeast Univ. Nat. Sci. Ed. 2023, 53, 857–868.
3. Guan M.Z., Guan K.S., Wang T.C. Summary of Shaking Table Test Research on Anti-Dipping Rock Slope. Earthq. Resist. Eng. Retrofit. 2021, 43, 157–167.
4. Guan G.F., Xiong W., Wang H. Control of a Dual Shaking Tables Vibration Test System. J. Vib. Shock 2017, 36, 207–211.
5. Li X., Wang J., Li F., et al. Differential Movement Synchronous Tracking Control Strategy of Double-Shaking Table System Loading with Specimen. Shock Vib. 2018, 2018, 1785184.
6. Yu H.T., Chen X.Z., Li P. Analytical Solution for Design Parameters of Model Box to Simulate Seismic Spatial Variability Effect Using Double-Array Shaking Tables. Chin. J. Geotech. Eng. 2020, 42, 1428–1434.
7. Wang J., Li F. Synchronous Tracking Control Strategy of Dual-Actuator Excited Shaking Table. Int. J. Struct. Stab. Dyn. 2025, 25, 2550215.
8. Hu S., Ren X., Zheng D., et al. Neural-Network-Based Robust Adaptive Synchronization and Tracking Control for Multimotor Driving Servo Systems. IEEE Trans. Transport. Electrif. 2024, 10, 9618–9630.
9. Wei Y., Xu Q. Design of a New Passive End-Effector Based on Constant-Force Mechanism for Robotic Polishing. Robot. Comput.-Integr. Manuf. 2022, 74, 102278.
10. Chen F., Zhao H., Li D., et al. Contact Force Control and Vibration Suppression in Robotic Polishing with a Smart End Effector. Robot. Comput.-Integr. Manuf. 2019, 57, 391–403.
11. Du H., Sun Y., Feng D., et al. Automatic Robotic Polishing on Titanium Alloy Parts with Compliant Force/Position Control. Proc. Inst. Mech. Eng. B J. Eng. Manuf. 2015, 229, 1125–1138.
12. Whitney D.E., Rourke J.M. Mechanical Behavior and Design Equations for Elastomer Shear Pad Remote Center Compliances. J. Dyn. Syst. Meas. Control 1986, 108, 223–232.
13. Li H., Liu X., Liu Y., et al. Research on Passive Compliance Control Method of High Altitude Wind Turbine Blade Grinding Robots Based on Improved ADRC. China Mech. Eng. 2025, 36, 1832.
14. Deng J.X., Yang B.Y., Huang Q.L., et al. Review on the Key Technologies of Complex Surfaces Polishing Based on Robots. J. Mech. Eng. 2024, 60, 1–21.
15. Ye S., Jiang B.G., Tian H., et al. Research on MRE Passive Compliant Device in Large Component Assembly. Mod. Manuf. Eng. 2024, 9, 34–39.
16. Zhang S., Sun Q., Hu J.C., et al. Arm-Wrist Hybrid Upper Limb Rehabilitation Robot Passive Compliance Control. Chin. J. Constr. Mach. 2024, 22, 468–473.
17. Wang L., Xie H., Wang Z. Configuration Design and Characteristics Research of an Inner Braced and Nested Assembly Manipulator with Dual Passive Compliance Characteristics. Robot 2024, 46, 105–117.
18. Liu Y.H., Chen L.J., Fang C.G., et al. Improved PID Control Method Based on Passive Compliance Device. Ind. Instrum. Autom. 2023, 6, 114–120.
19. Jiang Y.H., Chen C.J. Industrial Robot Teleoperation Assembly System Based on Force Feedback Equipment. J. Mech. Electr. Eng. 2025, 42, 137–145.
20. Liu X.F., Chen R., Wang B., et al. Dynamics Analysis and Control Strategy Research of More Redundantly Actuated Parallel Mechanism 2RPU+2UPR+RPR. J. Mech. Eng. 2024, 60, 237–249.
21. Chen K., Zhang S., Zhang J. Force/Position Hybrid Control for Cable-Driven Parallel Robots Based on the System Stiffness. J. Mech. Transmiss. 2023, 47, 130–134.
22. Zhang Z.H., Li W., Gao Z., et al. Force/Position Hybrid Control of Multi-Manipulator Based on Fuzzy Adaptive Sliding Mode Algorithm. J. Integr. Technol. 2023, 12, 72–81.
23. Yin W., Lian D., Li K., et al. Manipulator Force/Position Hybrid Control Based on Staged Adaptation. J. Beijing Univ. Aeronaut. Astronaut. 2025, 51, 161–166.
24. Hogan N. Impedance Control: An Approach to Manipulation. In Proceedings of the 1984 American Control Conference, Seattle, WA, USA, 6–8 June 1984; pp. 304–313.
25. Hogan N., Buerger S.P. Impedance and Interaction Control. In Robotics and Automation Handbook; CRC Press: Boca Raton, FL, USA, 2005.

 doi:10.20944/preprints202604.1109.v1

26. Xu L.Q., Wang X.W., Li M. A Study of Machine Manpower Tracking Based on Joint Torque Feedback under Impedance Control. Mech. Manag. Dev. 2024, 39, 36–37, 40.
27. Yang Z.H., Du C.H. Variable Impedance Control of Dual Pickup Robot Arm for Omnidirectional Movement of Tennis Robot. Mach. Des. Manuf. 2025, 5, 64–67.
28. Li L., Wang Z., Huang X. Research on Constant Force Control System of Robot Bonnet Polishing Based on Fuzzy Impedance Control. China Mech. Eng. 2025, 36, 1028.
29. Gong X.L., Xu Z. Research on the Control Method of the Flexible Grasping Force of the End of a Picking Robot under the Impedance Model. Ind. Instrum. Autom. 2024, 4, 52–56.
30. Haddadin S., Shahriari E. Unified Force-Impedance Control. Int. J. Robot. Res. 2024, 43, 2112–2141.
31. Bonitz R.C., Hsia T.C. Internal Force-Based Impedance Control for Cooperating Manipulators. IEEE Trans. Robot. Autom. 1996, 12, 78–89.
32. Ba K., Yu B., Gao Z., et al. An Improved Force-Based Impedance Control Method for the HDU of Legged Robots. ISA Trans. 2019, 84, 187–205.
33. Wang R.B. Active Compliance Control of 6-UPS Parallel Manipulator. Ph.D. Thesis, Nanjing University of Aeronautics and Astronautics, Nanjing, China, 2020.
34. Du Z.C. On the Active Compliant Control of a 2-DOF Parallel Manipulator. Ph.D. Thesis, Xidian University, Xi'an, China, 2022.
35. Lian L.J. Research on Precise Measurement and Control of an Electric 6-DOF Loading System. Ph.D. Thesis, Dalian University of Technology, Dalian, China, 2022.
36. Caccavale F., Chiacchio P., Marino A., et al. Six-DOF Impedance Control of Dual-Arm Cooperative Manipulators. IEEE/ASME Trans. Mechatron. 2008, 13, 576–586.
37. Ba K., Yu B., Gao Z., et al. Dynamic Compliance Analysis for LHDS of Legged Robot, Part B: Force-Based Impedance Control. IEEE Access 2018, 6, 74799–74811.
38. Gazi O. Understanding Digital Signal Processing; Springer: Cham, Switzerland, 2018.
39. Li Z., Liu J., Huang Z., et al. Adaptive Impedance Control of Human–Robot Cooperation Using Reinforcement Learning. IEEE Trans. Ind. Electron. 2017, 64, 8013–8022.
40. Gao Y., Wang J., Gao S., et al. An Integrated Robust Design and Robust Control Strategy Using the Genetic Algorithm. IEEE Trans. Ind. Inform. 2021, 17, 8378–8386.
41. Panicker S., Gostar A.K., Bab-Hadiashar A., et al. Tracking of Targets of Interest Using Labeled Multi-Bernoulli Filter with Multi-Sensor Control. Signal Process. 2020, 171, 107451.